

Complementary-Switchable Dual-Mode SHF Scandium-Aluminum Nitride BAW Resonator

Dicheng Mo, Student Member, IEEE, Shaurya Dabas, Student Member, IEEE, Sushant Rassay, Student Member, IEEE, and Roozbeh Tabrizian, Senior Member, IEEE

Abstract— This paper presents a bulk acoustic wave (BAW) resonator with complementary switchable operation in the first and second thickness extensional modes (TE_1 and TE_2) at 7.04 GHz and 13.4 GHz. Two ferroelectric scandium-aluminum nitride ($Sc_{0.28}Al_{0.72}N$) layers are alternatively stacked with three molybdenum electrodes, creating a laminated BAW resonator with independent switchability of polarization in constituent transducers. This enables intrinsic switchability of the resonator in TE_1 and TE_2 modes, when the ferroelectric $Sc_{0.28}Al_{0.72}N$ layers are poled in the same or opposite directions, respectively. A generalized analytical proof of complementary switchable operation, extended to laminated BAW resonators consisting of arbitrary number of $Sc_xAl_{1-x}N$ layers, is presented. For the demonstrated prototype, electromechanical coupling coefficients (k_t^2) of 10.1% and 10.7%, and quality factors (Q) of 115 and 151, are measured for TE_1 and TE_2 modes, respectively, when the resonator is configured in corresponding operation states. Besides showing intrinsically configurable operation in super-high-frequency regime with high k_t^2 and Q , laminated $Sc_{0.28}Al_{0.72}N$ BAW resonator exhibits repeatable operation under switching cycles.

Index Terms—Scandium aluminum nitride; ferroelectric; intrinsic switchability; complementary switchable; periodically poled; BAW resonator, super-high frequency.

I. Introduction

With the exponential increase in wireless data traffic, adaptive spectrum allocation becomes increasingly vital to avoid congestion and interference. Realization of adaptive spectrum allocation in wireless systems requires reconfigurable spectral processors that enable dynamic control over pass- and stop-bands at the radio frequency front-end (RFFE) [1-4].

Currently, the integrated RF duplexers and filters are created using aluminum nitride (AlN) surface and bulk acoustic wave (S/BAW) resonators. High quality-factor (Q) AlN BAW and SAW filter technologies with frequencies as high as 6 GHz are extensively adopted in RFFE of modern wireless systems [2-6]. These technologies, however, do not provide any intrinsic frequency tunability or switchability, and their operation is limited to a fixed band. Therefore, extension of communication

capacity, to enhance data rates and exploit uncongested spectrum in cm- and mm-wave regimes, requires arraying a large set of fixed-frequency filters using external switches to enable band selection and data aggregation. This strategy is not scalable considering the unfavorable increase in RFFE footprint with the addition of new filters, and excessive loss and power consumption of multiplexers needed for switching.

Alternative acoustic resonator technologies were proposed to achieve intrinsic configurability based on the use of perovskite ferroelectric and paraelectric transducers [7-11]. In these technologies the dependence of transducer polarization and acoustic velocity on DC electric field enables intrinsic switching and frequency tuning of the resonator. However, the major limitation of these technologies is their frequency scaling beyond the ultra-high-frequency regime (UHF: 0.3-3 GHz). This is due to the excessive electrical and mechanical loss of conventional perovskite and ferroelectric films and the processing challenges with thickness miniaturization upon extreme frequency scaling of the resonators.

The recent discovery of ferroelectricity in scandium-doped aluminum nitride films ($Sc_xAl_{1-x}N$) is poised to surpass the limitations of perovskites and enable intrinsically configurable resonators with extreme scaling to super-high-frequency regime (SHF: 3-30 GHz) [12]. Configurable thickness-mode BAW and intrinsically switchable Lamb-wave resonators with frequencies up to 10 GHz are recently demonstrated using ferroelectric $Sc_xAl_{1-x}N$ films [13-17]. In this paper, we present a novel SHF BAW resonator architecture based on laminating two $Sc_xAl_{1-x}N$ transducers with independent electrical control on their polarization direction. This architecture enables complementary-switchable operation of the resonator in different thickness-extensional mode harmonics (TE_i , $i = 1, 2$) with consistently large electromechanical coupling coefficient (k_t^2) and Q .

II. CONCEPT

Efficient excitation of acoustic resonance modes in piezoelectric transducers require harmonic alignment of mechanical stress profile and applied electric field. In conventional thickness-mode BAW resonators, the electric field is applied uniformly across the piezoelectric film thickness through the top and bottom metal electrodes. This architecture

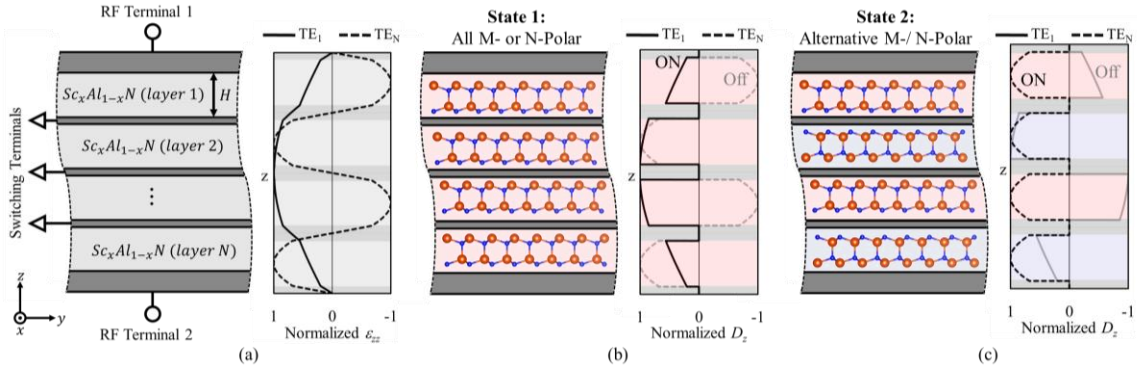


Fig. 1. (a) Schematic of a laminated BAW resonator structure with N $\text{Sc}_x\text{Al}_{1-x}\text{N}$ layers and $N+1$ metal layers, and the normalized z -axis strain for TE_1 and TE_N modes for $N = 4$. (b) State 1: the $\text{Sc}_x\text{Al}_{1-x}\text{N}$ layers in the resonator are uniformly M- or N- polar. The D_z is constructive for TE_1 and destructive for TE_N , resulting in maximum and 0 k_t^2 for TE_1 and TE_N , respectively. (c) State 2: $\text{Sc}_x\text{Al}_{1-x}\text{N}$ layers in the resonator are alternating between M- and N- polar. The D_z is destructive for TE_1 and constructive for TE_N , resulting in 0 and maximum k_t^2 for TE_1 and TE_N , respectively.

limits the electrically excitable acoustic modes to odd thickness-extensional and thickness-shear harmonics. Further, the k_t^2 of the higher-order odd modes decreases, proportional to the mode number, due to the excessive charge cancellation across the transducer thickness.

The laminated BAW resonator is created from alternative stacking of N $\text{Sc}_x\text{Al}_{1-x}\text{N}$ films with $N + 1$ metal layers (integer $N \geq 1$). This structure enables creation of a resonator with a single RF port and N isolated DC ports for independent polarization control of $\text{Sc}_x\text{Al}_{1-x}\text{N}$ films.

Figure 1(a) schematically shows the laminated BAW resonator structure, where the RF electric field is applied uniformly across the N $\text{Sc}_x\text{Al}_{1-x}\text{N}$ films through the top and bottom electrodes, while the intermediate electrodes enable independent control of the polarization direction in $\text{Sc}_x\text{Al}_{1-x}\text{N}$ layers based on the ferroelectric behavior. Figure 1(a) also shows the z -axis strain for the first and N^{th} ($N = 4$) thickness-extensional modes (*i.e.*, TE_1 and TE_N).

Reversing polarization direction, by applying low-frequency switching pulses [18, 19], enables 180° phase-shift in mechanical excitations. This facilitates excitation of both odd and even thickness modes with similarly large k_t^2 , despite the uniform electric field across all the $\text{Sc}_x\text{Al}_{1-x}\text{N}$ layers.

Assuming infinitesimally thin metal electrodes, the mode-shape function of the M^{th} thickness-extensional BAW mode (TE_M) in the lamination of N $\text{Sc}_x\text{Al}_{1-x}\text{N}$ layers with thickness of H is formulated by the normalized z -axis strain $\varepsilon_{zz,M}(z)$ as:

$$\varepsilon_{zz,M}(z) = \sin\left(\frac{M\pi}{NH}z\right) \quad (1).$$

Considering the linear dependence of the effective longitudinal piezoelectric coefficient ($e_{33,eff}$) in $\text{Sc}_x\text{Al}_{1-x}\text{N}$ on its instantaneous polarization (P_{inst}), the electric displacement ($D_{z,M}$) across the laminated stack is derived as:

$$D_{z,M}(z) = e_{33}P_{inst}(z)\varepsilon_{zz,M}(z) \quad (2).$$

Here, e_{33} is the longitudinal piezoelectric constant for a perfectly metal-polar (M-polar) $\text{Sc}_x\text{Al}_{1-x}\text{N}$ film. The motional charge per unit area ($Q_{m,M}$) is derived from:

$$\begin{aligned} Q_{m,M} &= \int_0^{NH} \frac{D_{z,M}(z)}{NH} dz \\ &= e_{33} \sum_{i=1}^N \int_{(i-1)H}^{iH} \frac{P_{inst,i}\varepsilon_{zz,M}(z)}{NH} dz \end{aligned} \quad (3).$$

Here, $P_{inst,i}$ is P_{inst} in the i^{th} $\text{Sc}_x\text{Al}_{1-x}\text{N}$ layer. Using Eq. (3), the k_t^2 of the TE_M mode can be derived as [20]:

$$k_{t,M}^2 = \frac{\frac{1}{2} \frac{Q_{m,M}^2}{C_0}}{\frac{1}{2} \frac{Q_{m,M}^2}{C_0} + \int_0^{NH} \frac{c_{33}}{2} \varepsilon_{zz,m}^2(z) dz} \quad (4).$$

Here, c_{33} is the z -axis elastic constant of $\text{Sc}_x\text{Al}_{1-x}\text{N}$, and C_0 is the laminate capacitance per unit area:

$$C_0 = \frac{\varepsilon_{33}}{NH} \quad (5),$$

where ε_{33} is the z -axis dielectric constant. Considering Eq. (3) and Eq. (4), $Q_{m,M}$ and $k_{t,M}^2$ can be maximized by proper switching of constituent $\text{Sc}_x\text{Al}_{1-x}\text{N}$ layers in the laminate to maximally harmonize $\varepsilon_{zz,M}$. Specifically, opting for uniform (*i.e.*, State 1: $P_{inst,i} = \pm 1$ for all i) or alternating (*i.e.*, State 2: $P_{inst,i} = (-1)^i$) poling of $\text{Sc}_x\text{Al}_{1-x}\text{N}$ layers, two optimum operation states is recognized.

A. Operation State 1: Uniform Polarization

Opting for uniform polarization direction in all $\text{Sc}_x\text{Al}_{1-x}\text{N}$ layers results in the highest k_t^2 for the TE_1 mode when inserting $P_{inst,i} = \pm 1$ in Eq. (3) and Eq. (4) and derived as:

$$\begin{aligned} k_{t,1}^2 &= \frac{\frac{e_{33}^2}{\varepsilon_{33}} \left(\int_0^{NH} \sin\left(\frac{\pi z}{NH}\right) dz \right)^2}{\frac{e_{33}^2}{\varepsilon_{33}} \left(\int_0^{NH} \sin\left(\frac{\pi z}{NH}\right) dz \right)^2 + \int_0^{NH} \frac{c_{33}}{2} \left(\sin\left(\frac{\pi z}{NH}\right) \right)^2 dz} \\ &= \frac{8}{\pi^2} \cdot \frac{e_{33}^2}{\varepsilon_{33}c_{33}} \cdot \frac{1}{1 + \frac{8}{\pi^2} \cdot \frac{e_{33}^2}{\varepsilon_{33}c_{33}}} \end{aligned} \quad (6).$$

In this operation state, the motional charge of the TE_N mode ($Q_{m,N}$) is nulled considering:

$$Q_{m,N} = e_{33} \int_0^{NH} \sin\left(\frac{N\pi z}{NH}\right) dz = 0 \quad (7).$$

This results in a k_t^2 of 0 for the TE_N mode. Besides the TE_I mode, it should be noted that higher odd harmonics (*i.e.*, $M = 2a + 1$; a is a positive integer) can also be excited in this operation state. However, the k_t^2 of these harmonics is significantly lower than the TE_I mode and is derived using Eq. (6) and Eq. (7) as:

$$k_{t,2a+1}^2 = \frac{k_{t,1}^2}{(2a + 1)^2} \quad (8).$$

These harmonics may appear as spurious bands, when the resonator is used for spectral processing in RFFE. Considering the low k_t^2 and distant location in frequency spectrum, these spurious bands can be concealed by proper filter design.

B. Operation State 2: Alternating Polarization

On the other hand, opting for alternating polarization switching of the layers in laminate (*i.e.*, State 2: $P_{inst,i} = (-1)^i$) results in perfectly constructive accumulation of motional charge for the TE_N mode considering:

$$Q_{m,N} = e_{33} \sum_{i=1}^N \int_{(i-1)H}^{iH} (-1)^i \sin\left(\frac{\pi}{H}z\right) dz \\ = N \int_0^H \sin\left(\frac{\pi}{H}z\right) dz \quad (9).$$

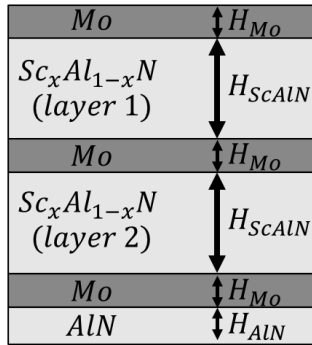
This results in a maximum k_t^2 for TE_N mode derived as:

$$k_{t,N}^2 = \frac{\frac{e_{33}^2}{\epsilon_{33}} \left(N \int_0^H \sin\left(\frac{\pi}{H}z\right) dz \right)^2}{\frac{e_{33}^2}{\epsilon_{33}} \left(N \int_0^H \sin\left(\frac{\pi}{H}z\right) dz \right)^2 NH + c_{33} \int_0^{NH} \epsilon_{zz,N}^2(z) dz} \\ = \frac{8}{\pi^2} \cdot \frac{e_{33}^2}{\epsilon_{33} c_{33}} \cdot \frac{1}{1 + \frac{8}{\pi^2} \cdot \frac{e_{33}^2}{\epsilon_{33} c_{33}}} \quad (10).$$

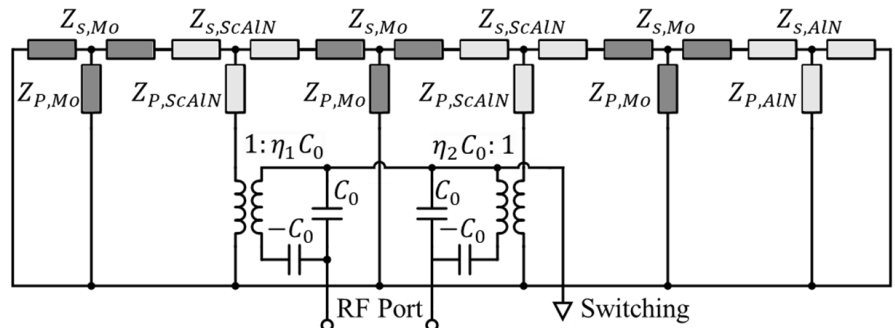
In this operation state, the motional charge, $Q_{m,1}$, for the TE_I mode is derived as:

$$Q_{m,1} = e_{33} \sum_{i=1}^N \int_{(i-1)H}^{iH} (-1)^i \epsilon_{zz,M}(z) dz = \\ \frac{e_{33}}{2} \sum_{i=1}^N (-1)^i \left(\int_{(i-1)H}^{iH} \epsilon_{zz,1}(z) dz + \int_{(N-i)H}^{(N-i+1)H} \epsilon_{zz,1}(z) dz \right) \quad (11).$$

Replacing TE_I mode z -axis strain $\epsilon_{zz,1}$ and using auxiliary



(a)



(b)

Fig. 2. (a) Cross-section schematic of the proposed laminated BAW resonator highlighting constituent layers and their thickness. (b) The Mason's waveguide model for the laminated BAW resonator corresponding to the stack shown in Fig. 2(a).

variable $\hat{z} = NH - z$, Eq. (10) can be simplified using:

$$\int_{(N-i)H}^{(N-i+1)H} \sin\left(\frac{\pi}{NH}z\right) dz \& = - \int_{(i-1)H}^{iH} \sin\left(\frac{\pi}{NH}(NH - \hat{z})\right) d\hat{z} \\ = - \int_{(i-1)H}^{iH} \sin\left(\frac{\pi}{NH}\hat{z}\right) d\hat{z} \quad (12).$$

Inserting Eq. (12) in Eq. (11), $Q_{m,1}$ is nulled. This results in a k_t^2 of 0 for the TE_I mode, when operating in State 2.

This proves the complementary operation of the resonator in TE_I and TE_N modes, when the stack polarization is configured in uniform (State 1) or alternating (State 2) states, respectively. In this paper, laminated $Sc_xAl_{1-x}N$ BAW resonators with $N = 2$ layers and complementary switchable operation in TE_1 and TE_2 modes is demonstrated.

It should also be noted that in State 2, besides the TE_N mode, only higher-order harmonics with $M = N(2a + 1)$ can be excited. The k_t^2 of these modes is derived using Eq. (6) and Eq. (7) as:

$$k_{t,N(2a+1)}^2 = \frac{k_{t,N}^2}{(2a + 1)^2} \quad (13).$$

The complementary operation principle is schematically demonstrated in Fig. 1(b-c), showing the electric displacement for TE_I and TE_N ($N = 4$) modes in the two operation states. In State 1 (Fig. 1(b)), all the $Sc_xAl_{1-x}N$ layers are all either metal- (*i.e.*, M-polar: Sc or Al) or nitrogen-polar (*i.e.*, N-polar), resulting in transduction of the TE_I and suppression of TE_N modes. In State 2 (Fig. 1(c)), the $Sc_xAl_{1-x}N$ layers are alternating between M- and N-polar resulting in suppression of TE_I and transduction of TE_N modes.

III. RESONATOR MODELING AND DESIGN

In presence of electrodes with finite thicknesses, the operation of laminated $Sc_xAl_{1-x}N$ BAW resonator can be modeled using the Mason's waveguide approach [21]. Figure 2(a) schematically shows the cross-section of the resonator reported in this paper, consisting of two 150nm-thick $Sc_xAl_{1-x}N$ layers, three 50nm-thick molybdenum (Mo) electrodes, stacked atop of 58.5nm-thick AlN seed layer. Figure 2(b) shows the resonator Mason's model consisting of cascaded waveguides representing the laminate layers. In this model $Z_{s,i}$ and $Z_{p,i}$ are

TABLE 1.

MATERIAL PROPERTIES AND THICKNESSES OF LAYERS IN LAMINATED $\text{Sc}_x\text{Al}_{1-x}\text{N}$ BAW RESONATOR, USED FOR MODELING.				
Parameter	Mo	Al	$\text{Sc}_{0.28}\text{Al}_{0.72}\text{N}$	AlN
Layer Thickness (nm)	50	50	145	58
Acoustic Impedance ($10^6 \text{ Pa}\cdot\text{s}/\text{m}$)	66.38	17.39	31.27	35.83
BAW Velocity (m/s)	6,508	6,441	8,808	10,857
e_{33} (C/m^2)	-	-	2.15	1.55
Relative Permittivity	-	-	20.6	9

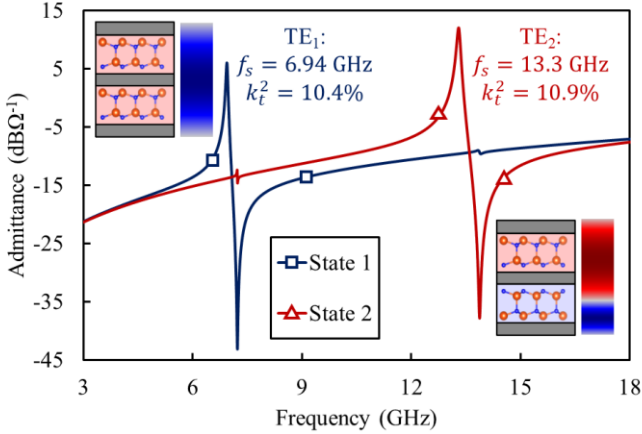


Fig. 3. Simulated admittance of the laminated resonator, using Mason's model. In State 1 the $\text{Sc}_{0.28}\text{Al}_{0.72}\text{N}$ layers are uniformly poled, resulting in transduction of TE_1 and suppression of TE_2 . In State 2 the $\text{Sc}_{0.28}\text{Al}_{0.72}\text{N}$ layers are poled in opposite direction, resulting in transduction of TE_2 and suppression of TE_1 .

the series and shunt acoustic impedance of the layer i ($i \in \{\text{Mo}, \text{ScAlN}, \text{AlN}\}$) in the laminate and formulated as:

$$\begin{aligned} Z_{s,i} &= jZ_i \tan(\beta_i d_i / 2), \\ Z_{p,i} &= -jZ_i / \sin(\beta_i d_i) \end{aligned} \quad (14).$$

Here, Z_i , β_i and d_i are the acoustic impedance per unit area, the wavenumber, and the thickness of corresponding layers, defined by z -axis elastic constant ($c_{33,i}$) and mass-density (ρ_i) of each layer and the operation frequency (f) as:

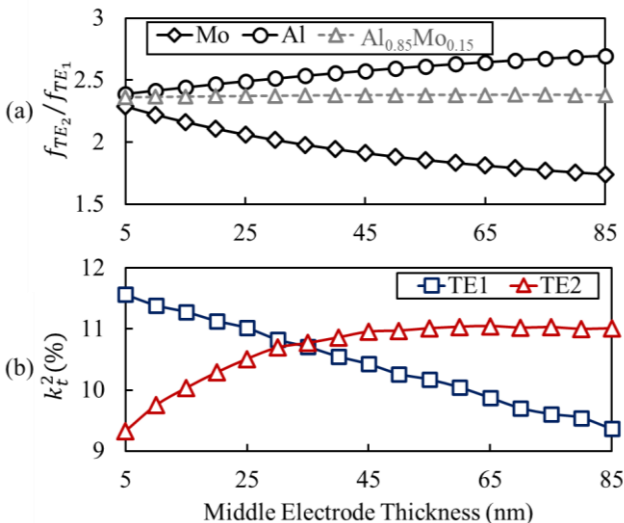


Fig. 4. (a) Simulated frequency ratio of TE_1 and TE_2 modes for different center electrode materials and thicknesses. (b) Simulated k_t^2 of TE_1 and TE_2 modes for different thicknesses of Mo center-electrode.

$$\begin{aligned} Z_i &= c_{33,i} \beta_i / (2\pi f), \\ \beta_i &= (2\pi f) / \sqrt{c_{33,i} / \rho_i} \end{aligned} \quad (15).$$

The configurable operation of the resonator is modeled using the polarization-dependent piezoelectric coefficient (*i.e.*, $e_{33,eff,i} = e_{33} P_{inst,i}$) for the transformers representing electromechanical transduction (η_i) and in $\text{Sc}_x\text{Al}_{1-x}\text{N}$ layers as:

$$\eta_i = e_{33} P_{inst,i} / \epsilon_{33} \quad (16).$$

Finally, the static capacitors per unit area corresponding to each $\text{Sc}_x\text{Al}_{1-x}\text{N}$ layers is derived as:

$$C_0 = \epsilon_{33} / d_i \quad (17).$$

Figure 3 shows the simulated admittance of the resonator, using the material properties and layer thicknesses listed in Table 1 for the constituent layers, assuming a top-electrode area of $6,500 \mu\text{m}^2$. In State 1 (*i.e.*, $P_{inst,1} = P_{inst,2}$), TE_1 is excited at 6.94 GHz, with a k_t^2 of 10.4%, while TE_2 is suppressed. Alternatively, in State 2 (*i.e.*, $P_{inst,1} = -P_{inst,2}$), TE_2 is excited at 13.3 GHz with a k_t^2 of 10.9%, while TE_1 is suppressed.

The frequency ratio of TE_1 and TE_2 modes for this structure is 1.92. This ratio can be accurately controlled by changing the thickness or material of the middle electrode layer. Figure 4(a) shows the TE_1 and TE_2 frequency ratio as a function of the middle electrode thickness for aluminum (Al) and Mo. When using Mo, the thickness of the middle electrode can be optimized to achieve an integer ratio of 2. Having a resonator with complementary-switchable modes with integer ratio is highly desirable for sub- and super-harmonic communication schemes that are used for enhancement of data rate and reduction of latency in congested wireless networks [22, 23]. Further, using Mo-Al alloy, with 15% Mo atomic fraction, for the middle electrode enables sustaining a constant frequency ratio across large thickness variations that may result from process uncertainties. Finally, it should be noted that the change in middle electrode thickness has an opposite effect on the k_t^2 of TE_1 and TE_2 modes, considering the contrasted z -axis strain profile of the two modes at the center of the laminate. Figure 4(b) shows the k_t^2 of TE_1 and TE_2 modes for different thicknesses of Mo middle electrode. Using proper thickness (34nm), the same k_t^2 of 10.8% can be achieved for both modes.

IV. DEVICE FABRICATION

Figure 5 shows the fabrication process for creation of laminated $\text{Sc}_{0.28}\text{Al}_{0.72}\text{N}$ BAW resonators. The process consists of successive deposition and patterning of $\text{Sc}_{0.28}\text{Al}_{0.72}\text{N}$ and Mo layers on a silicon (Si) substrate. $\text{Sc}_{0.28}\text{Al}_{0.72}\text{N}$ are deposited using reactive magnetron sputtering from segmented scandium-aluminum targets [18]. Mo layers are deposited using DC sputtering. Prior to deposition of the first Mo layer, a $\sim 58\text{nm}$ AlN layer is deposited to serve as the seed, enabling (110)-textured growth of Mo film [24]. This further helps c -axis textured-growth of $\text{Sc}_{0.28}\text{Al}_{0.72}\text{N}$ films.

Figure 6(a) shows the cross-sectional scanning electron microscope (SEM) image of the stack, highlighting the thickness of constituent layers in the laminate. Prior to deposition of the first $\text{Sc}_{0.28}\text{Al}_{0.72}\text{N}$ layer, the bottom Mo is patterned using boron trichloride (BCl_3) gas in an inductively

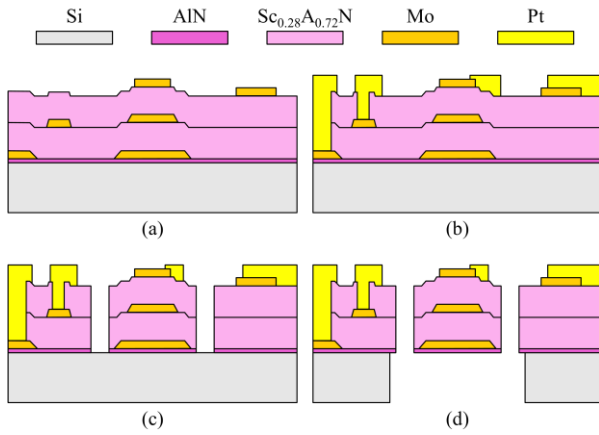


Fig. 5. Fabrication process for creation of laminated $\text{Sc}_{0.28}\text{Al}_{0.72}\text{N}$ BAW resonators: (a) Deposition and patterning of transducer. (b) Etching access to bottom and metal electrodes and metallization. (c) Etching trenches to define lateral geometry. (d) Releasing device from backside.

coupled plasma reactive-ion-etching (RIE ICP) system. The bottom Mo electrode is patterned using tapered photoresist mask features created by proximity exposure mode photolithography. This enables formation of Mo patterns with slanted sidewalls, which is essential for crack-free growth of successive $\text{Sc}_{0.28}\text{Al}_{0.72}\text{N}$ layers. A similar procedure is repeated to pattern middle Mo electrodes and prior to deposition of the second $\text{Sc}_{0.28}\text{Al}_{0.72}\text{N}$ layer. Figure 6(b) shows

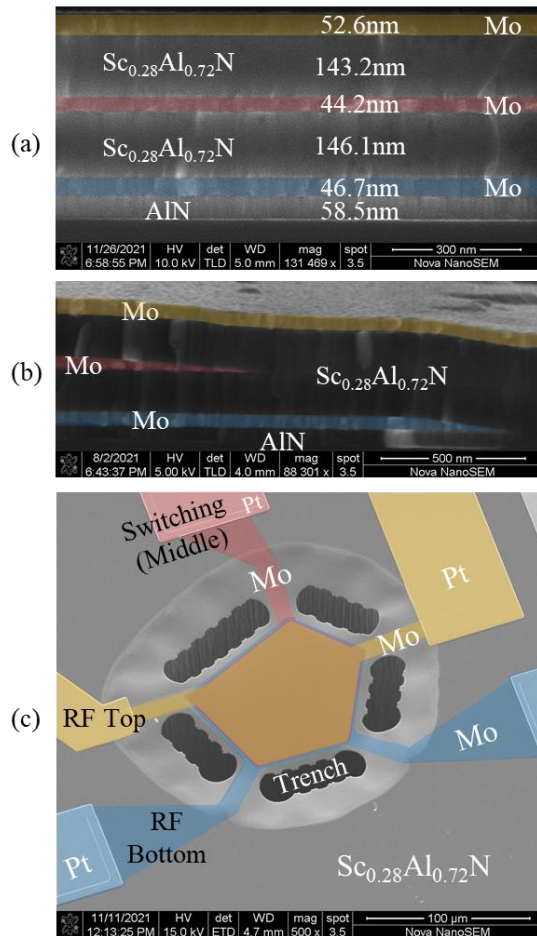


Fig. 6. (a) Cross-sectional SEM of (a) the laminated $\text{Sc}_{0.28}\text{Al}_{0.72}\text{N}$ transducer and (b) at the edge of patterned electrodes, highlighting the smooth slanted sidewalls and crack-free $\text{Sc}_{0.28}\text{Al}_{0.72}\text{N}$ growth. (c) SEM image of complementary switchable $\text{Sc}_{0.28}\text{Al}_{0.72}\text{N}$ BAW resonator.

the cross-sectional SEM of the transducer stack at the edge of patterned bottom and middle Mo electrodes, highlighting the slanted sidewall and crack-free texture of $\text{Sc}_{0.28}\text{Al}_{0.72}\text{N}$ layers.

To evaluate the crystal quality and degree of c -axis orientation, X-ray omega scans (*i.e.*, rocking curves) are performed after deposition of each $\text{Sc}_{0.28}\text{Al}_{0.72}\text{N}$ layer on patterned Mo electrodes. Full-width-half-maximums (FWHM) of 2.33° and 2.64° are measured for (002) $\text{Sc}_{0.28}\text{Al}_{0.72}\text{N}$ after deposition of the first and second $\text{Sc}_{0.28}\text{Al}_{0.72}\text{N}$ layers, respectively. The higher FWHM measured after the deposition of second layer may correspond to slight shift in diffraction peak angle due to the different residual stress in top and bottom $\text{Sc}_{0.28}\text{Al}_{0.72}\text{N}$ films.

After deposition of the second $\text{Sc}_{0.28}\text{Al}_{0.72}\text{N}$ layer and the third Mo layer, the top electrodes are patterned using a similar etch process as bottom and middle Mo layers, but with photoresist mask created in contact mode lithography, to achieve straight walls.

Following deposition of the transducer stack, the $\text{Sc}_{0.28}\text{Al}_{0.72}\text{N}$ layers are etched using a timed chlorine-hydrogen ($\text{Cl}_2\text{-H}_2$) based recipe in RIE ICP system to reach bottom and middle Mo electrodes. Next, 500nm-thick platinum (Pt) layer is deposited and patterned using lift-off to create routing lines and pads. The resonator lateral geometry is then patterned using silicon-dioxide hard-mask and BCl_3 recipe in ICP RIE. Finally, the resonators are released by deep-reactive-ion-etching of Si handle layer from the backside of the substrate. Figure 6(c) shows the SEM image of the laminated $\text{Sc}_{0.28}\text{Al}_{0.72}\text{N}$ BAW resonator. The RF and switching terminals are highlighted.

V. CHARACTERIZATION

Laminated $\text{Sc}_{0.28}\text{Al}_{0.72}\text{N}$ BAW resonators are measured to characterize their switching behavior and RF characteristics. Ferroelectric polarization hysteresis and switching behavior of the constituent $\text{Sc}_{0.28}\text{Al}_{0.72}\text{N}$ layers are characterized using a Radiant PiezoMEMS ferroelectric tester. Resonator RF performance is measured using Keysight N5222A PNA vector network analyzer (VNA), along with short-open-load-through (SOLT) calibration procedure enabled by the designated kits. The resonator nonlinearity is measured using two Keysight N5173B signal generators for two-tone input signal excitation and a Keysight N9010A signal analyzer, with a $20\text{dB} \pm 1.2\text{dB}$ attenuator, for harmonic detection. Finally, the temperature characteristic of frequency is extracted by measuring resonator in a temperature-controlled Semi-Probe PSL4 RF probe station.

A. Ferroelectric Characterization

The polarization hysteresis loop of the 150nm-thick $\text{Sc}_{0.28}\text{Al}_{0.72}\text{N}$ layers in the laminate is measured by driving the ferroelectric film using 20kHz bipolar triangular signals with 80V amplitude and measuring instantaneous current. Figure 7(a) shows the measured polarization-voltage hysteresis loop for the top $\text{Sc}_{0.28}\text{Al}_{0.72}\text{N}$ layer, used for resonator switching between TE_1 and TE_2 modes. A coercive voltage of 79V is measured, highlighting the large voltage required for polarization switching of the film. The polarization and coercive voltage are on par with previous report for $\text{Sc}_x\text{Al}_{1-x}\text{N}$

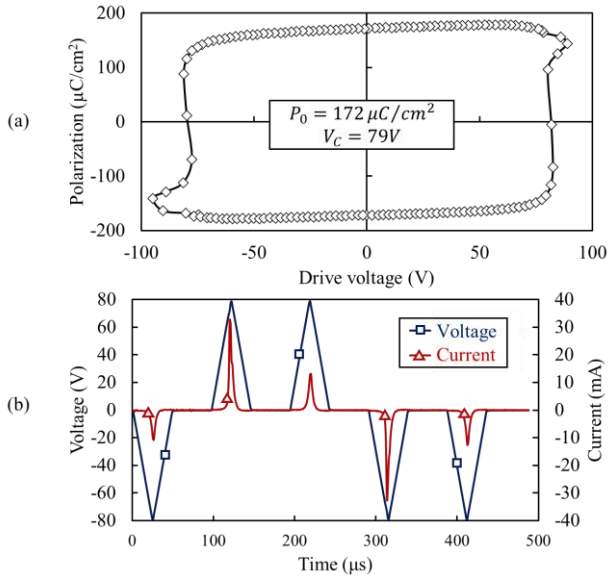


Fig. 7. (a) Measured polarization-voltage hysteresis loop for the top $\text{Sc}_{0.28}\text{Al}_{0.72}\text{N}$ layer, used for resonator switching, highlighting a coercive voltage of 79V. (b) The polarization switching procedure using triangular voltage pulses, and the corresponding polarization switching current, peaking at pulse-sign transitions.

film with similar Sc content and compressive residual stress [12]. Figure 7(b) shows the measured instantaneous current for the bipolar triangular pulse-train drive that is used for polarization switching between M- and N-polar states. The large current at the transition between positive and negative triangular pulses is induced by the polarization switching. While the application of 80V enables switching with a single pulse, opting for smaller voltages results in partial switching and facilitates observation of resonator response evolution as transitioning between the two states.

B. Admittance Measurement

The resonator admittance is extracted from the measured reflection coefficient (*i.e.*, S_{11}). Figure 8(a) shows the large-span admittance of the laminated $\text{Sc}_{0.28}\text{Al}_{0.72}\text{N}$ BAW resonator in two operation states. In State 1, both $\text{Sc}_{0.28}\text{Al}_{0.72}\text{N}$ layers are poled in the same direction (M-polar in Fig. 8(a)), resulting in excitation of TE_1 and suppression of TE_2 modes. Upon application of 20kHz triangular switching pulses to the bottom $\text{Sc}_{0.28}\text{Al}_{0.72}\text{N}$ layer, the resonator reconfigures to State 2, where the TE_1 mode is suppressed and TE_2 emerges. Figure 8(b-c) show the short-span admittance when operating in each state, highlighting the evolution across inter-state transition. Using $\sim 78\text{V}$ switching voltage, the transition is obtained by application of 5 pulses. Figure 8(b-c) insets show the performance metrics of TE_1 and TE_2 modes, in State 1 and State 2, respectively. k_t^2 and Q values are using [25, 26]:

$$k_t^2 = \frac{\pi^2}{8} \left(\frac{f_p^2 - f_s^2}{f_s^2} \right), Q = \frac{f}{2} \left| \frac{\partial \varphi_Y}{\partial f} \right| \quad (18).$$

Here f_s and f_p are the series and parallel resonance frequencies and φ_Y is admittance phase. In State 1, TE_1 operates at 7.04 GHz with a Q of 115 and k_t^2 of 10.1%. In State 2, TE_2 operates at 13.4 GHz with a Q of 151 and k_t^2 of 10.7%.

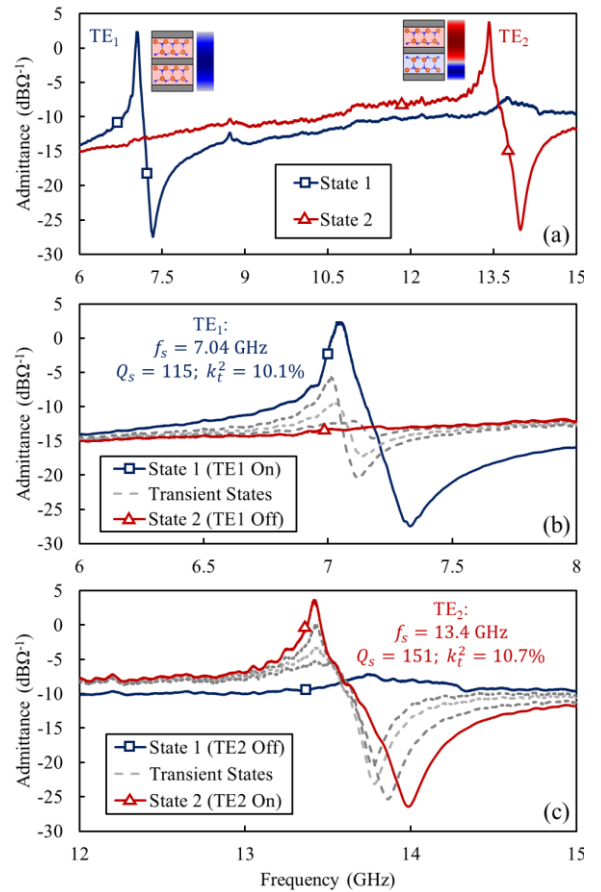


Fig. 8. (a) Measured large-span admittance of the complementary switchable SHF $\text{Sc}_{0.28}\text{Al}_{0.72}\text{N}$ BAW resonator in two operation states. State 1 (uniform polarization of $\text{Sc}_{0.28}\text{Al}_{0.72}\text{N}$ layers) the TE_1 is on and TE_2 is off. Switching to State 2 (alternating polarization of $\text{Sc}_{0.28}\text{Al}_{0.72}\text{N}$ layers) turns off the TE_1 mode and turns on the TE_2 mode. Measured short-span admittance of (a) TE_1 and (b) TE_2 modes, as evolving from State 1 to State 2 by application of switching pulse.

C. Retention under Switching

The performance retention of the resonator is measured under 50 switching cycles. Figure 9 shows the variations in frequency, Q and k_t^2 of the TE_1 mode over switching. Early in the switching cycles (*i.e.*, after the first 5 cycles), a slight drop is observed in frequency and k_t^2 . This may correspond to fractional domain wall pinning and due to defects and imperfect intergranular boundaries [27, 28], which induce undesirable charge cancellation in $\text{Sc}_{0.28}\text{Al}_{0.72}\text{N}$ transducer. After these initial degradations, a stable operation is observed with frequency fluctuations within 0.11%, and Q and k_t^2 variations within 7.4% and 3.7%, respectively. Similar to other ferroelectric devices, the performance retention in switchable $\text{Sc}_{0.28}\text{Al}_{0.72}\text{N}$ BAW resonators can be significantly improved by enhancing crystallinity of the film and reduction of defects.

D. Nonlinearity and Temperature Characteristics

The nonlinearity of laminated $\text{Sc}_{0.28}\text{Al}_{0.72}\text{N}$ BAW resonator is measured using two tones with 10MHz frequency offset. Figure 10(a) shows the nonlinearity characteristic of the resonator, highlighting second- and third-order input intercept point (*i.e.*, IIP2 and IIP3) for the TE_1 mode of 59.5 dBm and 40.5 dBm, respectively. These values are comparable with UHF AlN BAW counterparts [29, 30]. The apparent lower slope for

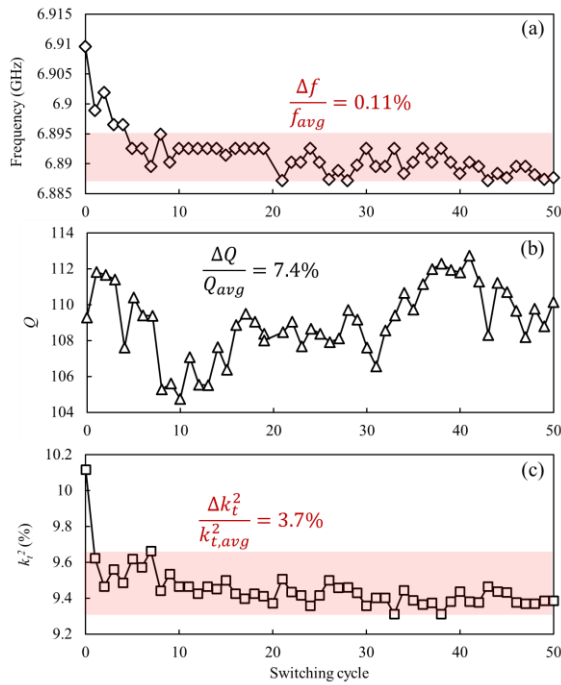


Fig. 9. Measured retention characteristic of $\text{Sc}_{0.28}\text{Al}_{0.72}\text{N}$ BAW resonator's (a) frequency, (b) Q , and (c) k_t^2 , over 50 switching cycles.

intermodulation (IM) at lower end of the input power corresponds to the small magnitude of the third harmonic that is nearly buried by the noise floor of measurement setup. Figure 10(b) shows the measured temperature characteristics of TE_1 and TE_2 modes frequency, over -20°C to 100°C . Linear temperature coefficient of frequency (TCF) of -43.49 ppm/ $^\circ\text{C}$

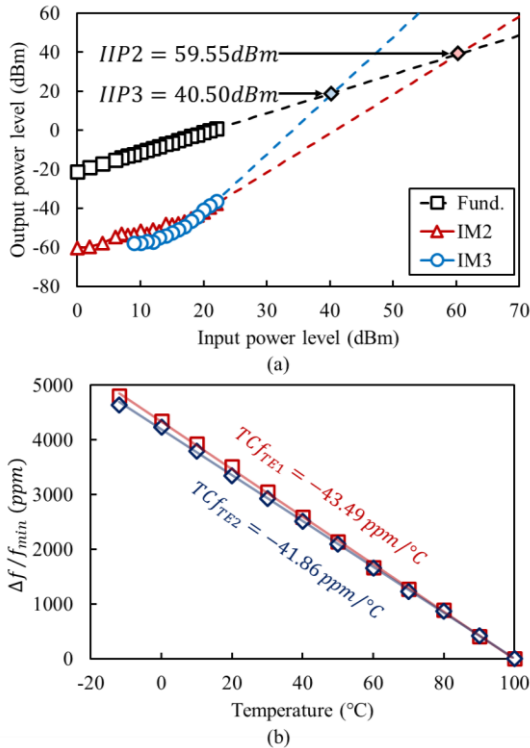


Fig. 10. (a) Measured nonlinearity characteristic of the TE_1 mode. The output power is measured with a $20\text{dB} \pm 1.2\text{dB}$ attenuator to protect the spectrum analyzer. (b) Measured temperature characteristic of TE_1 and TE_2 modes frequency.

and -41.86 ppm/ $^\circ\text{C}$ are measured for TE_1 and TE_2 modes, respectively. The slightly higher temperature sensitivity of TE_1 mode may correspond to the placement of middle Mo in high-strain region of the mode-shape and the large negative temperature coefficient of elasticity of Mo [31].

VI. CONCLUSION

This paper presented a new $\text{Sc}_x\text{Al}_{1-x}\text{N}$ BAW resonator technology with complementary-switchable operation in fundamental and high-order thickness extensional modes (*i.e.*, TE_1 and TE_N). The resonator structure consists of N ferroelectric $\text{Sc}_x\text{Al}_{1-x}\text{N}$ films alternatively stacked with $N + 1$ metal electrodes, enabling independent polarization switching of each piezoelectric film. Opting for uniform or alternating poling of the $\text{Sc}_x\text{Al}_{1-x}\text{N}$ layers, the resonator can be switched to operate in two complementary states with either TE_1 or TE_N active resonance modes of similarly large k_t^2 . The generalized principle of complementary-switchable operation in laminated $\text{Sc}_x\text{Al}_{1-x}\text{N}$ BAW resonators were formulated and the role of ferroelectric polarization tuning in excitation and suppression of fundamental and harmonic BAW modes were discussed. Resonator prototype implemented in a laminate consisting of two 150nm-thick $\text{Sc}_{0.28}\text{Al}_{0.72}\text{N}$ layers and three $\sim 50\text{nm}$ Mo layers was presented. The resonator was switched by application of 20kHz triangular pulses to either operate in the TE_1 mode, at 7.04GHz with a Q of 115 and k_t^2 of 10.1%, or in the TE_2 mode, at 13.4 GHz with a Q of 151 and k_t^2 of 10.7%. The performance retention of the resonator under 50 switching cycles were presented highlighting repeatable operation after a slight degradation in frequency and k_t^2 in the initial cycles. The resonator nonlinearity, when operating in TE_1 mode, was measured showing IIP2 and IIP3 of 59.55dBm and 40.50dBm, respectively. The temperature characteristic of TE_1 and TE_2 modes was measured showing a TCF of -43.49 ppm/ $^\circ\text{C}$ and -41.86 ppm/ $^\circ\text{C}$, respectively. The presented complementary-switchable super-high-frequency BAW resonator was well-suited for creation of intrinsically configurable spectral processors in modern wireless systems and congested networks.

ACKNOWLEDGMENT

The authors would like to thank the University of Florida Nanoscale Research Facility cleanroom staff for fabrication support and Troy Tharpe for the help with crystal structure modeling.

REFERENCES

- [1] M. Matthaiou, O. Yurduseven, H. Q. Ngo, D. Morales-Jimenez, S. L. Cotton and V. F. Fusco, "The Road to 6G: Ten Physical Layer Challenges for Communications Engineers," in *IEEE Communications Magazine*, vol. 59, no. 1, pp. 64-69, January 2021, doi: 10.1109/MCOM.001.2000208.
- [2] R. Ruby, "A Snapshot in Time: The Future in Filters for Cell Phones," in *IEEE Microwave Magazine*, vol. 16, no. 7, pp. 46-59, Aug. 2015, doi: 10.1109/MMM.2015.2429513.
- [3] S. Mahon, "The 5G Effect on RF Filter Technologies," in *IEEE Transactions on Semiconductor Manufacturing*, vol. 30, no. 4, pp. 494-499, Nov. 2017, doi: 10.1109/TSM.2017.2757879.
- [4] M. Schaefer, R. Rothmund and G. Fattinger, "Process and Design Challenge for SMR-type Bulk Acoustic Wave (BAW) Filters at Frequencies Above 5 GHz," *2019 IEEE International Ultrasonics*

- Symposium (IUS)*, 2019, pp. 1696-1699, doi: 10.1109/ULTSYM.2019.8925767.
- [5] D. Kim, G. Moreno, F. Bi, M. Winters, R. Houlden, D. Aichele and J.B. Shealy, "Wideband 6 GHz RF Filters for Wi-Fi 6E Using a Unique BAW Process and Highly Sc-doped AlN Thin Film," *2021 IEEE MTT-S International Microwave Symposium (IMS)*, 2021, pp. 207-209, doi: 10.1109/IMS19712.2021.9574981.
 - [6] K. Karnati, M. Schaefer, W. Yusuf, R. Rothemund, M. Al-Joumayly and G. Fattinger, "5G C-V2X Filter Using BAW Technology," *2021 IEEE MTT-S International Microwave Filter Workshop (IMFW)*, 2021, pp. 109-111, doi: 10.1109/IMFW49589.2021.9642350.
 - [7] M. Z. Koohi and A. Mortazawi, "Negative piezoelectric-based electric-field-actuated mode-switchable multilayer ferroelectric FBARs for selective control of harmonic resonances without degrading K_{eff}^2 ," *IEEE Trans. Ultrason. Ferroelectr. Freq. Control*, vol. 67, no. 9, pp. 1922-1930, Sep. 2020, doi: 10.1109/TUFFC.2020.2988632.
 - [8] Y. He, B. Bahr, M. Si, P. Ye and D. Weinstein, "A tunable ferroelectric based unreleased RF resonator," *Microsyst. Nanoeng.*, vol. 6, no. 1, pp. 1-7, Dec. 2020, doi: 10.1038/s41378-019-0110-1.
 - [9] M. Z. Koohi, W. Peng and A. Mortazawi, "An intrinsically switchable balanced ferroelectric FBAR filter at 2 GHz," *IEEE MTT-S Int. Microw. Symp. Dig.*, pp. 131-134, Aug. 2020, doi: 10.1109/IMS30576.2020.9223799.
 - [10] H. Chandrahilim, S. A. Bhave, R. G. Polcawich, J. S. Pulskamp and R. Kaul, "PZT transduction of high-overtone contour-mode resonators," *IEEE Trans. Ultrason. Ferroelectr. Freq. Control*, vol. 57, no. 9, pp. 2035-2041, Sep. 2010, doi: 10.1109/TUFFC.2010.1651.
 - [11] S. V. Ptashnik, A.K. Mikhailov, A.V. Yastrebov, P.K. Petrov, W. Liu, N.M. Alford, S. Hirsch and A.B. Kozyrev, "Ferroelectric thin film acoustic devices with electrical multiband switching ability," *Scientific Reports* vol.7, no.1, pp. 1-10, Nov. 2017, doi: 10.1038/s41598-017-14895-8.
 - [12] S. Fichtner, N. Wolff, F. Lofink, L. Kienle, and B. Wagner, "AlScN: A III-V semiconductor based ferroelectric," *J. Appl. Phys.*, vol. 125, no. 11, Mar. 2019, Art. no. 114103, doi: 10.1063/1.5084945.
 - [13] M. Park, Z. Hao, D. G. Kim, A. Clark, R. Dargis and A. Ansari, "A 10 GHz Single-Crystalline Scandium-Doped Aluminum Nitride Lamb-Wave Resonator," *2019 20th International Conference on Solid-State Sensors, Actuators and Microsystems & Eurosensors XXXIII (TRANSDUCERS & EUROSENSORS XXXIII)*, 2019, pp. 450-453, doi: 10.1109/TRANSDUCERS.2019.8808374.
 - [14] S. Rassay, D. Mo, C. Li, N. Choudhary, C. Forgey and R. Tabrizian, "Intrinsically Switchable Ferroelectric Scandium Aluminum Nitride Lamb-Mode Resonators," in *IEEE Electron Device Letters*, vol. 42, no. 7, pp. 1065-1068, July 2021, doi: 10.1109/LED.2021.3078444.
 - [15] J. Wang, Y. Zheng, and A. Ansari, "Ferroelectric aluminum scandium nitride thin film bulk acoustic resonators with polarization-dependent operating states," *Phys. Status Solidi (RRL) Rapid Res. Lett.*, vol. 15, no. 5, May 2021, Art. no. 2100034, doi: 10.1002/pssr.202100034.
 - [16] Z. A. Schaffer, G. Piazza, S. Mishin and Y. Oshmyansky, "Super High Frequency Simple Process Flow Cross-Sectional Lamé Mode Resonators in 20% Scandium-Doped Aluminum Nitride," *2020 IEEE 33rd International Conference on Micro Electro Mechanical Systems (MEMS)*, 2020, pp. 1281-1284, doi: 10.1109/MEMS46641.2020.9056279.
 - [17] S. Rassay, F. Hakim, M. Ramezani and R. Tabrizian, "Acoustically Coupled Wideband RF Filters with Bandwidth Reconfigurability Using Ferroelectric Aluminum Scandium Nitride Film," *2020 IEEE 33rd International Conference on Micro Electro Mechanical Systems (MEMS)*, 2020, pp. 1254-1257, doi: 10.1109/MEMS46641.2020.9056353.
 - [18] S. Rassay, F. Hakim, C. Li, C. Forgey, N. Choudhary & R. Tabrizian, "A Segmented-Target Sputtering Process for Growth of Sub-50 nm Ferroelectric Scandium-Aluminum-Nitride Films with Composition and Stress Tuning," *Physica Status Solidi (RRL)-Rapid Research Letters* vol. 15, no.5, pp. 2100087, May. 2021, doi: 10.1002/pssr.202100087.
 - [19] S. Dabas, D. Mo, S. Rassay and R. Tabrizian, "Intrinsically Tunable Laminated Ferroelectric Scandium Aluminum Nitride Extensional Resonator Based on Local Polarization Switching," *2022 IEEE 35th International Conference on Micro Electro Mechanical Systems Conference (MEMS)*, 2022, pp. 1050-1053, doi: 10.1109/MEMS51670.2022.9699790.
 - [20] J. F. Rosenbaum, *Bulk acoustic wave theory and devices*, Artech House Acoustics Library, 1988.
 - [21] W. P. Mason, *Physical Acoustics Principles and Methods*, vol. 1A. New York: Academic Press, 1964.
 - [22] D. Lopez-Diaz, I. Kallfass, A. Tessmann, A. Leuther, S. Wagner, M. Schlechtweg and O. Ambacher, "A subharmonic chipset for gigabit communication around 240 GHz," *2012 IEEE/MTT-S International Microwave Symposium Digest*, 2012, pp. 1-3, doi: 10.1109/MWSYM.2012.6258404.
 - [23] D. Kumar, S. Mondal, Y. Deng, and P. Chahal, "Wireless battery-free harmonic communication system for pressure sensing," *Micromachines* vol. 11, no. 12, pp: 1043, Dec. 2020, doi: 10.3390/mi11121043.
 - [24] V. Felmetger, M. Mikhov, M. Ramezani and R. Tabrizian, "Sputter Process Optimization for Al_{0.7}Sc_{0.3}N Piezoelectric Films," *2019 IEEE International Ultrasonics Symposium (IUS)*, 2019, pp. 2600-2603, doi: 10.1109/ULTSYM.2019.8925576.
 - [25] R. Lu, M. -H. Li, Y. Yang, T. Manzanique and S. Gong, "Accurate Extraction of Large Electromechanical Coupling in Piezoelectric MEMS Resonators," in *Journal of Microelectromechanical Systems*, vol. 28, no. 2, pp. 209-218, Apr. 2019, doi: 10.1109/JMEMS.2019.2892708.
 - [26] D. A. Feld, R. Parker, R. Ruby, P. Bradley and S. Dong, "After 60 years: A new formula for computing quality factor is warranted," *2008 IEEE Ultrasonics Symposium*, 2008, pp. 431-436, doi: 10.1109/ULTSYM.2008.0105.
 - [27] A. Bencan, G. Drazic, H. Ursic, M. Makarovic, M. Komelj and T. Rojac, "Domain-wall pinning and defect ordering in BiFeO₃ probed on the atomic and nanoscale." *Nature communications* vol.11, no.1, pp. 1-9, Apr. 2020, doi: 10.1038/s41467-020-15595-0.
 - [28] A. Abdollahi and I. Arias. "Numerical simulation of intergranular and transgranular crack propagation in ferroelectric polycrystals." *International journal of fracture*, vol.174, no.1, pp. 3-15, Mar. 2012, doi: 10.1007/s10704-011-9664-0.
 - [29] H. Campanella, Y. Qian, C. O. Romero, J. S. Wong, J. Giner and R. Kumar, "Monolithic Multiband MEMS RF Front-End Module for 5G Mobile," in *Journal of Microelectromechanical Systems*, vol. 30, no. 1, pp. 72-80, Feb. 2021, doi: 10.1109/JMEMS.2020.3036379.
 - [30] R. Aigner, N. -H. Huynh, M. Handtmann and S. Marksteiner, "Behavior of BAW devices at high power levels," *IEEE MTT-S International Microwave Symposium Digest*, 2005., 2005, pp. 429-432, doi: 10.1109/MWSYM.2005.1516620.
 - [31] J. M. Dickinson and P. E. Armstrong, "Temperature dependence of the elastic constants of molybdenum," *Journal of applied Physics* vol. 38, no. 2, pp. 602-606, Feb. 1967, doi: 10.1063/1.1709381.